Spatiotemporal mode structure of nonlinearly coupled drift wave modes

Christian Brandt,* Olaf Grulke, and Thomas Klinger
Max-Planck-Institut für Plasmaphysik, Wendelsteinstraße 1, D-17489 Greifswald, Germany

José Negrete Jr.
Max-Planck-Institut für Dynamik und Selbstorganisation, Am Faßberg 17, D-37077 Göttingen, Germany

Guillaume Bousselin, Frédéric Brochard, and Gérard Bonhomme
Jean-Lamour Institute, Unité Mixte de Recherche No. 7198 associée au Centre National de la Recherche Scientifique, Henri Poincaré University, Boîte Postale No. 70239, F-54506 Vandoeuvre-lès-Nancy, France

Stella Oldenbürger
Itoh Research Center for Plasma Turbulence, Kyushu University, Kasuga, Japan
(Received 8 July 2011; revised manuscript received 24 September 2011; published 11 November 2011)

This paper presents full cross-section measurements of drift waves in the linear magnetized plasma of the Mirabelle device. Drift wave modes are studied in regimes of weakly developed turbulence. The drift wave modes develop azimuthal space-time structures of plasma density, plasma potential, and visible light fluctuations. A fast camera diagnostic is used to record visible light fluctuations of the plasma column in an azimuthal cross section with a temporal resolution of 10 μs corresponding approximately to 10% of the typical drift wave period. Mode coupling and drift wave dispersion are studied by spatiotemporal Fourier decomposition of the camera frames. The observed coupling between modes is compared to calculations of nonlinearly coupled oscillators described by the Kuramoto model.

DOI: 10.1103/PhysRevE.84.056405 PACS number(s): 52.35.Mw, 52.35.Ra, 52.35.Kt, 05.45.Xt

I. INTRODUCTION

Over the past two decades drift waves have been extensively studied in the framework of anomalous energy and particle transport in magnetized plasmas designed for nuclear fusion [1,2]. Drift waves are basically density and potential fluctuations with dynamics parallel and perpendicular to the ambient magnetic field. A common diagnostic for drift waves is the Langmuir probe, which provides a spatially localized measurement of density, temperature, and potential. In particular, probe arrays arranged in the azimuthal or poloidal direction are now well established to study the drift wave dynamics perpendicular to the magnetic field [3–5]. However, probe arrays covering the full plasma cross section are too complex to build and would create a strong perturbation to the plasma. Here the (noninvasive) fast camera diagnostic represents a complementary diagnostic to Langmuir probes by measuring light fluctuations in the entire perpendicular cross section [6]. The camera measurements can be directly used for investigations of the dynamics of drift waves due to the high degree of correlation between light and density fluctuations in low-temperature plasmas [7,8]. During the past few years the temporal resolution of fast cameras has permanently increased with increasing quantum efficiencies of the complementary metal oxide semiconductor sensors. Nowadays, the frame rate is high enough to resolve drift wave dynamics. The spatial resolution perpendicular to the magnetic field can easily go below the millimeter range, depending on the parameters of the optics. The resolution parallel to the magnetic field, i.e., along the lines of sight of the camera, depends on the optical system. The optics used in the present work is a usual objective, which sharply images objects within a certain distance; however, the plasma is an expanded transparent light-emitting medium and thus a large part of the plasma is beyond the focused object distance. The farther away the light is from the focused object distance, the more blurred the picture is and thus light is more spread out on the camera chip. Taking this effect into account and according to the integration along the lines of sight, the main light contribution originates from a localized region with some lengths of the depth of field around the focused object distance. Consequently, the fast camera diagnostic provides all means to study drift wave turbulence including the nonlinear coupling between drift wave modes.

Various models for drift wave coupling have been proposed and developed further [9,10]. Three-wave coupling is a major mechanism of energy transfer between modes [11]. The spatiotemporal Fourier decomposition of camera frames is a useful tool for investigations on the dispersion and mode coupling of drift waves. This method is used in the present paper. It is shown that periodic pulling, synchronization, and desynchronization due to mode coupling in turbulence can be reproduced by the Kuramoto model for a set of nonlinearly coupled oscillators [12]. The Kuramoto model has been used to model the transition from incoherent to coherent states for ensembles of coupled flashing fireflies, spiking neurons, and pulsing dictyostelium discoideum cells [13–15]. It has been investigated for several years with focus on the thermodynamic limit $N \to \infty$ (i.e., an infinite number of oscillators), where closed solutions have been found for the time evolution of an oscillator ensemble with unimodal frequency distributions [16]. Recently, the Kuramoto model has been used to investigate the effects of connection topology in small-world networks; it has been found that a single

*christian.brandt@ipp.mpg.de

link between interacting clusters can be crucial to make a transition into a coherent state [17]. Despite the simplicity of the model, its behavior has been proven to be nontrivial and its understanding has attracted a lot of attention during the past decade [18].

The present paper is organized as follows. First we discuss drift waves in the cylindrical plasma device Mirabelle and the fast camera as a diagnostic for the spatiotemporal dynamics of drift waves. Then we investigate the dispersion relation and the mode coupling in weakly developed drift wave turbulence based on Fourier decomposition of azimuthal light fluctuation measurements. Finally, the drift wave mode coupling is compared to the Kuramoto model.

A. Experimental device

The drift wave experiments are conducted in the linearly magnetized plasma of the cylindrical device Mirabelle [19], depicted in Fig. 1. The device consists of two identical cylindrical chambers at both ends (0.7 m long, 0.9 m in diameter) and a cylindrical midsection 0.3 m in diameter and 1.4 m long. In the midsection a set of 24 magnetic field coils creates a homogeneous magnetic field with a magnetic field induction up to 130 mT.

One of the large chambers is used for generating helium plasma by a thermionic hot cathode discharge. Emitted electrons are accelerated toward the grid, which is biased positively with V_{ga} relative to the surrounding anode. In front of the grid a limiter (with a hole diameter of 15 cm) is used to reduce the diameter of the plasma column. In the midsection fast electrons ionize the gas and create a magnetized plasma column. The typical neutral gas pressure is

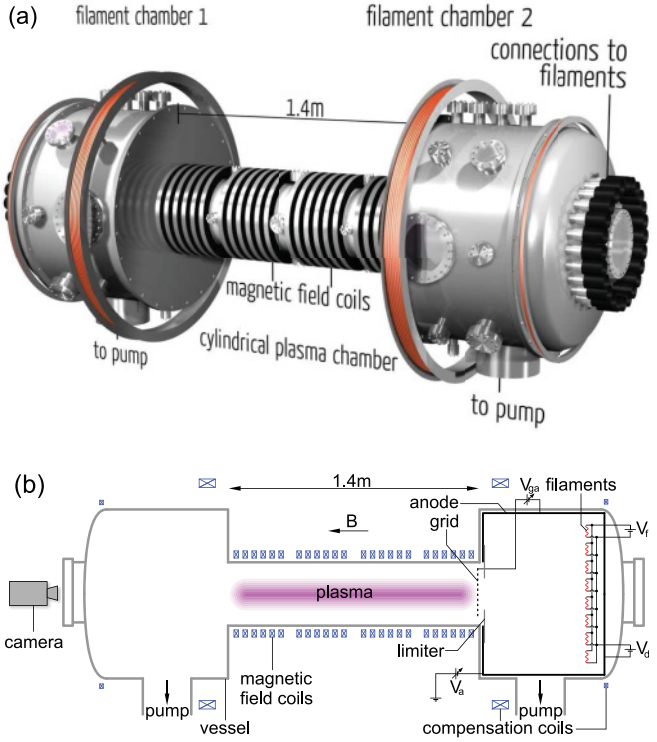

FIG. 1. (Color online) Thermionic plasma device Mirabelle: (a) three-dimensional drawing and (b) schematic.

$p = 2 \times 10^{-2}$ Pa. The peak electron density is approximately equal to 3×10^{16} m^{-3} and the peak electron temperature is approximately equal to 5 eV.

The plasma is diagnosed by a fast camera of the type Photron FASTCAM SA1.1. It is positioned in front of one end chamber [Fig. 1(b)], opposite the filament chamber, and aligned parallel to the plasma column. The camera focus is set to the middle of the plasma column, i.e., to a distance of $g = 1.5$ m. The objective has a diameter of 50 mm, a focal length of $f = 50$ mm, and the lens f-number is $\kappa = 1.2$ (maximum aperture). The distance between the nearest and farthest point where an object appears sharp is the depth of field L. It is given by $L = 2gd_h(g - f)/[d_h^2 - (g - f)^2]$ and yields 4.18 cm. The quantity $d_h = f^2(\kappa\sigma)^{-1}$ is the hyperfocal distance with $\sigma = 20$ μm being the width of one pixel (the criterion for the maximum diameter of the circle of confusion). The camera records the transparent light-emitting plasma by integration along the lines of sight. For a rough estimation of the region from where most of the light comes to the camera, the energy detected by one single pixel is calculated in dependence on the distance between the camera and a light-emitting object. Figure 2 depicts the diameter of the circle of confusion as well as the fraction of emitted energy that arrives at the camera lens. The width of the light-emitting object is assumed to be 0.58 mm (the spatial resolution in the focused object distance), the total emitted energy into the spherical wave is E_0, and thus the fraction of energy at the camera lens $E(z)/E_0$ decreases proportionally to z^{-2}. Finally, the energy detected by one pixel is a combination of the z^{-2} dependence and the diameter of the circle of confusion, i.e., $E(z)(\pi r_{cc}^2)^{-1}$. It peaks at the focused object distance and has a width (full width at half maximum) in the range of the depth of field. For larger light-emitting objects the peak broadens due to a superposition of neighboring circles of confusion. However, for structures in the plasma of a typical size of approximately 1 cm the calculation gives a rough estimation of the region. Consequently, most of the collected light originates from a region of approximately 30% of the plasma column around the focused object distance. The camera has a dynamic range of 12 bits and a maximum frame rate of $f = 675$ kHz. The

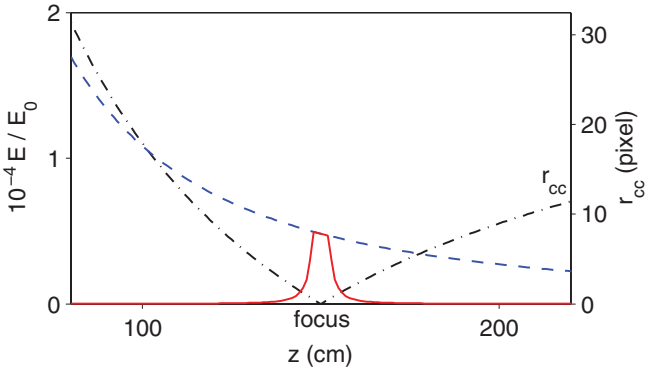

FIG. 2. (Color online) Localization of the recorded emitted light. The dash-dotted (black) line shows the radius of the circle of confusion r_{cc} and the dashed (blue) line is the energy of a light-emitting object arriving at the camera lens. The energy per pixel is a combination of both curves (red), i.e., $[E(z)/E_0](\pi r_{cc}^2)^{-1}$.

number of recording pixels on the chip as well as the collected light decreases with increasing frame rate. As a compromise between exposure time, temporal resolution, and the number of pixels, a frame rate of 90 kHz with an exposure time of 11.1 μs is used with a recording chip size of 200 × 200 pixels.

The experiments shown in Refs. [7,8] give evidence that light fluctuations recorded by the camera are well correlated with plasma electron density fluctuations. It is demonstrated that the major part of the light emission originates from transitions in excited neutral atoms. Generally speaking, the line intensity of an excited neutral atom is proportional to $n_j n_e \langle v_e(T_e)\sigma_{jk}(T_e)\rangle$, with $n_j = n_0$ being the neutral density, n_e the electron density, and σ_{jk} the cross section of a transition from state $j = 0$ to k. The neutral density can be regarded as spatially and temporally constant due to the low ionization degree in the thermionic discharge (≈0.02%). Furthermore, temperature fluctuations are negligible in the Mirabelle device [20]. Neutral atoms, once excited to the first metastable level by impact with high-energy electrons, can be excited to a next higher level by impact with low-energy electrons (1–5 eV) from the plasma bulk. Since the effective mean free path length of primary electrons is smaller than the length of the plasma column, the density of primary electrons is already considerable reduced in the observed plasma volume. This is supported by the strong correlation between measured radial ion saturation current profiles and radial light profiles [21].

B. Drift waves in the Mirabelle device

In the magnetized plasma column of the Mirabelle device midsection drift waves have been extensively studied [22–25]. Typical operation and plasma parameters used for the present investigations are listed in Table I.

The drift wave instability occurs in the region of density and temperature gradients. The density profile of the plasma is a flat-top type with a hollow shape, resulting in a density gradient length $L_n \approx -9$ cm at a radius $r = 3$ cm. The temperature profile is a Gaussian distribution and exhibits a gradient length $L_T \approx 4.5$ cm. In contrast to the flute mode instability, drift waves exhibit a finite parallel wavelength that is basically determined by the plasma resistivity and the sheaths at the end plates [26,27]. Here the parallel wavelength of drift waves in a helium plasma is measured by two axially separated Langmuir probes positioned on one magnetic field line. The measurement yields a parallel wavelength of (1.8 ± 0.1) m. The minimal perpendicular wavelength covered by the camera diagnostic is, according to the pixel resolution of 0.8 mm/pixel, approximately 3 mm. The covered mode numbers in the density gradient region ($r = 3.2$ cm) are $m \approx 1$–80 and in the core plasma ($r = 0.5$ cm) $m = 1$–10. The strongest observed coherent mode numbers are up to $m = 4$ in a frequency range between 1 and 15 kHz.

Figure 3(a) shows the frequency spectrum of ion saturation current fluctuations of a coherent $m = 3$ drift wave mode at $f = 4.5$ kHz. The spectrum of the light fluctuations [Fig. 3(b)] peaks at the same frequency. The amplitude is smaller relative to the background level due to the low signal-to-noise ratio of camera measurements. A snapshot of the light fluctuations observed in the azimuthal cross section is shown in Fig. 3(c), which clearly displays an $m = 3$ mode. The light fluctuation level correlates with the density and temperature gradient; it is zero in the center and peaks at $r = 3$ cm, the region of maximum density and temperature gradient. Both the normalized density and light fluctuation level are about 5% in the maximum gradient region. A time series of an azimuthal pixel array in the gradient region, taken from the camera frames, yields the space-time diagram depicted in Fig. 3(d). The slope of the phase fronts indicates the azimuthal velocity of the $m = 3$ mode. Similar space-time diagrams are obtained from density fluctuation measurements using Langmuir probe arrays [3–5].

TABLE I. Typical plasma and operational parameters of the plasma device Mirabelle. Quantities with a radial dependence are given in the plasma center. CF denotes collision frequency.

Parameter	Value	Unit
column length l	1.4	m
magnetic field B	57	mT
neutral gas pressure p_{He}	0.19	Pa
electron density n_e	$\lesssim 3 \times 10^{16}$	m^{-3}
electron temperature T_e	≈1–5	eV
ion temperature T_i	< 0.05	eV
plasma β	1.5×10^{-5}	
Debye length λ_D	85	μm
drift scale ρ_s	7.15	mm
electron gyroradius r_{ce}	0.12	mm
ion gyroradius r_{ci}	1.13	mm
ion plasma frequency ω_{pi}	1.1×10^8	rad/s
electron plasma frequency ω_{pe}	9.8×10^9	rad/s
ion cyclotron frequency ω_{ci}	1.4×10^6	rad/s
electron cyclotron frequency ω_{ce}	1.0×10^{10}	rad/s
electron-neutral CF ν_{ne}	3.1×10^6	s^{-1}
electron-ion CF ν_{ei}	1.5×10^5	s^{-1}
ion-neutral CF ν_{ni}	3.1×10^4	s^{-1}

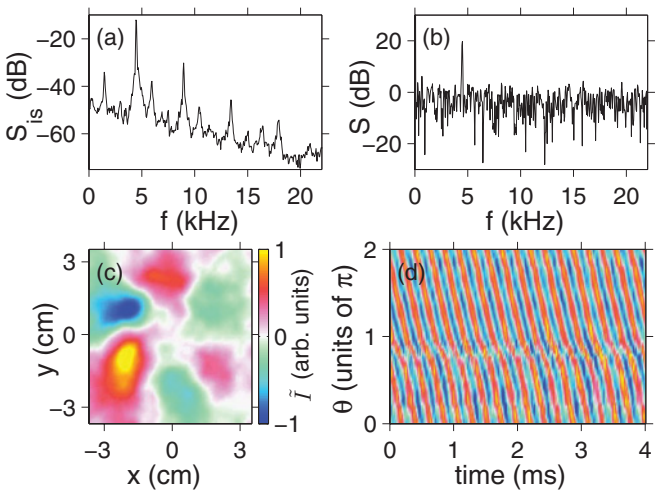

FIG. 3. (Color online) Spectra of (a) ion saturation current fluctuations and (b) visible light fluctuations of a coherent $m = 3$ drift wave mode. (c) Mode structure of light fluctuations in the azimuthal cross section. (d) Space-time diagram of an azimuthal camera pixel array at $r = 3$ cm.

The azimuthal propagation of drift waves is proportional to the electron diamagnetic drift. The frequency measured by a fixed probe is given by Ref. [28]

$$\omega_{\mathrm{dw}}(r,m) = \frac{-\boldsymbol{e}_z k_B T_e k_\perp}{eB\left(1+k_\perp^2\rho_s^2\right)}(\partial_r \ln n + \partial_r \ln T_e), \qquad (1)$$

where k_B is the Boltzmann constant, $T_e(r)$ is the electron temperature, e is the elementary charge, B is the magnetic induction, $\rho_s = (m_i T_e/eB^2)^{1/2}$ is the drift scale, $k_\perp(r,m) = m/r$ is the perpendicular wave number, and $n(r)$ is the density. Generally speaking, the wave propagation in the laboratory frame is Doppler shifted by the $E \times B$ drift $\boldsymbol{\omega}_{E\times B} = -\boldsymbol{e}_z \partial_r \phi/B$ caused by the background potential profile $\phi(r)$. In thermionic discharges the electric potential profile is often parabolic, resulting in a rigid-body rotation of the plasma column [24,29]. The potential profile in the Mirabelle device plasmas depends basically on the magnetic induction B and the diameter of the limiter [20]. The smaller the diameter of the limiter, the stronger the radial potential gradient and the $E \times B$ drift are. Finally, the measured drift wave frequency in the laboratory frame is

$$\boldsymbol{\omega} = \boldsymbol{\omega}_{\mathrm{dw}} + m\boldsymbol{\omega}_{E\times B}. \qquad (2)$$

II. MODE STRUCTURE OF WEAKLY DEVELOPED DRIFT WAVE TURBULENCE

Since the camera recordings allow for measurements of the spatiotemporal drift wave structure in an azimuthal cross section the camera movies are used to decompose the fluctuations in a weakly developed turbulent state into individual mode numbers to study the coupling across the individual spatial scales. The mode decomposition is done by the extraction of azimuthal pixel arrays for each radius and the calculation of the Fourier transform. Figure 4 shows the Fourier decomposition of a camera frame at one time instant [Fig. 4(a_1)] into its first six modes $m = 1-6$ [Figs. 4(b_1)–(g_1)]. An inverse Fourier transform of the first six modes yields, in a good approximation, the camera frame picture. The decomposed mode structures show a maximum fluctuation level at the position of maximum density and temperature gradient ($r = 3$ cm), while in the center the fluctuation level is zero. The $m = 2$ mode has the largest amplitude, followed by the modes $m = 1$ and 3. For larger mode numbers the amplitude decreases monotonically.

All decomposed modes show a spiral-like structure with the same winding direction. In time the mode structures propagate into the counterclockwise direction. The bottom row of Fig. 4 shows the radial profiles of the squared intensity of light fluctuations, which corresponds to the energy of the drift wave fluctuations. The profiles peak at a radial position and decay to zero toward the center and to larger radii. The width of the profiles decreases with increasing mode numbers. For the mode numbers $m = 1-5$ the radial positions of the maxima increase with increasing mode number. This is in agreement with calculations and measurements of drift waves in cylindrical geometry [30–32].

The mode amplitudes vary with time. An increase of a certain mode number leads to a decrease of another mode number. Figure 5 depicts the time evolution of the decomposed modes $m = 1-3$ of four consecutive camera frames. During a time interval $\tau = 33$ μs the total fluctuation energy of each mode changes. While the amplitude of the mode $m = 1$ decreases, the amplitudes of the modes $m = 2$ and 3 increase. The modes propagate in the same azimuthal direction, although core fluctuations propagate more slowly than edge fluctuations. Thus phase defects of the modes occur periodically at different radii between the center and the gradient region. For example, the mode $m = 2$ splits radially at $r \approx 1.5$ cm [Figs. 5(e) and 5(f)] and then two radially separated azimuthal modes,

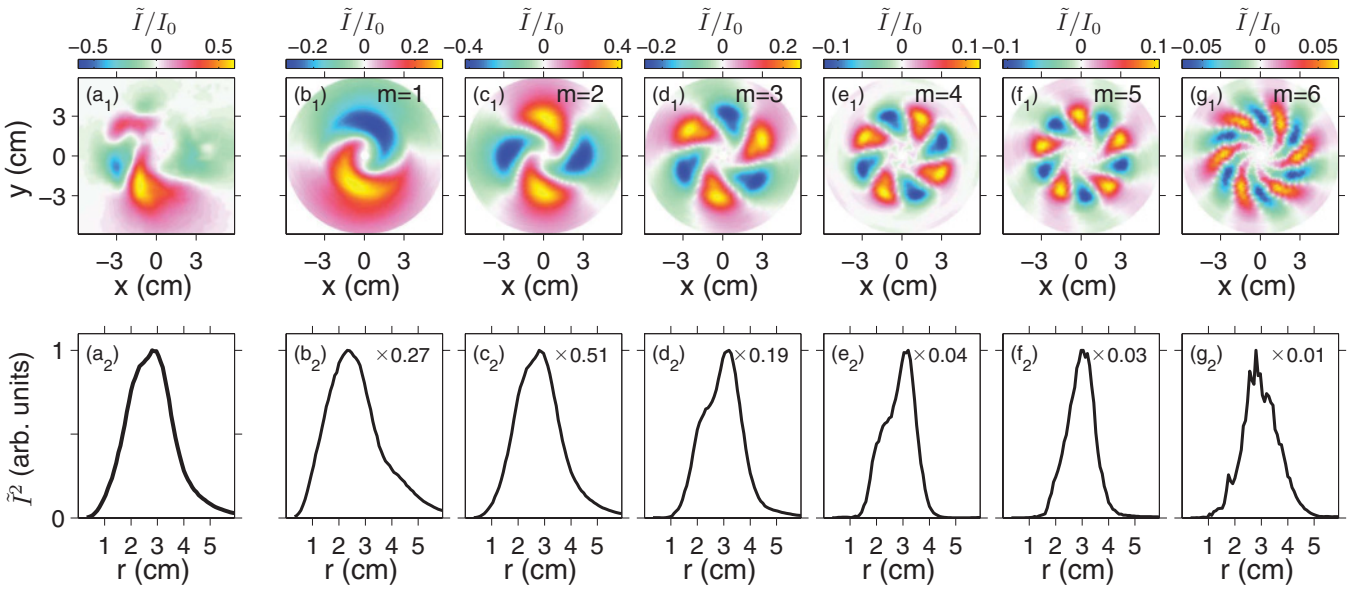

FIG. 4. (Color online) Fourier decomposition of one camera frame recording weakly developed drift wave turbulence. The first row shows the light fluctuations in the azimuthal cross section and the second row shows the corresponding radial fluctuation amplitude profiles for (a) the camera measurement and (b)–(g) the decomposed modes $m = 1-6$. The propagation direction of the mode structures is counterclockwise.

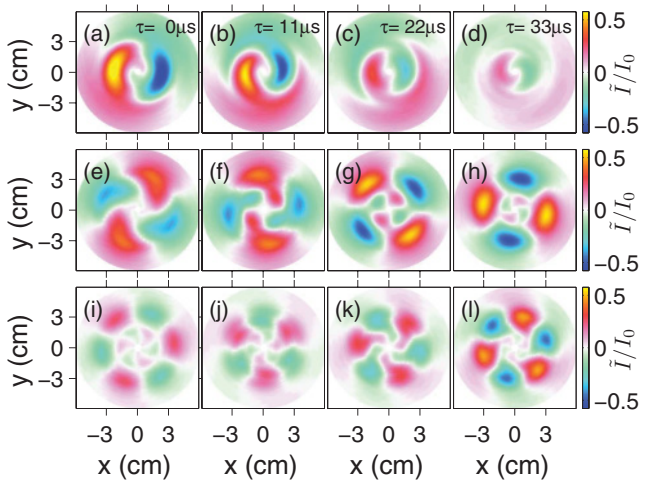

FIG. 5. (Color online) Time evolution of the decomposed modes (a)–(d) $m = 1$, (e)–(h) $m = 2$, and (i)–(l) $m = 3$. Each mode starts from the same camera frame.

a $m = 2$ mode close to the center and one in the gradient region, propagate independently. As a result, the amplitude of the outer $m = 2$ mode increases and the amplitude of the inner $m = 2$ mode decreases [Figs. 5(g) and 5(h)]. This is also observed for the other decomposed modes (for example, for $m = 3$ [Figs. 5(k) and 5(l)]). The modes are not pure azimuthal eigenmodes but exhibit radial components due to the radial phase defects and the spiral-like mode structure. Figure 6 shows the average mode-number spectrum of the spatiotemporal time series (the average over 400 ms). The spectrum is flat for small mode numbers, $m = 1-3$, and then decreases with $k^{-3.0}$ before it reaches the noise level at about $m = 17$. Most of the fluctuation energy is contained in the large scale modes. The number of interacting modes is low and the spectrum is not completely flat for low mode numbers ($m = 2$ is dominant). To distinguish the state of the investigated plasma from fully developed turbulence, we call it *weakly developed turbulence*, as it has been used in Refs. [29,33]. In turbulence the presence of several mode numbers at the same time allows, with the use of the camera diagnostic, for the measurement of

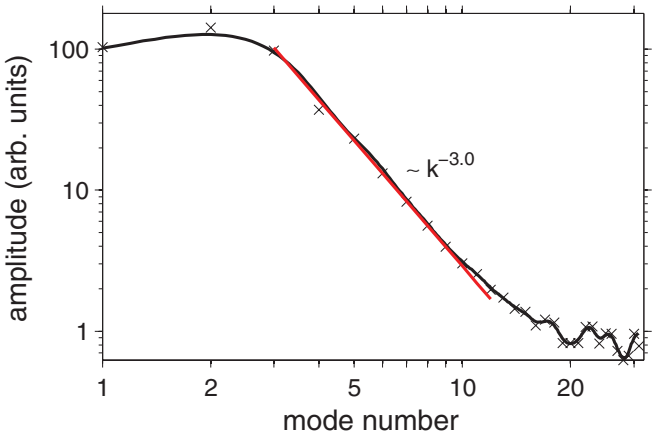

FIG. 6. (Color online) Average mode-number spectrum of weakly developed drift wave turbulence in a helium plasma.

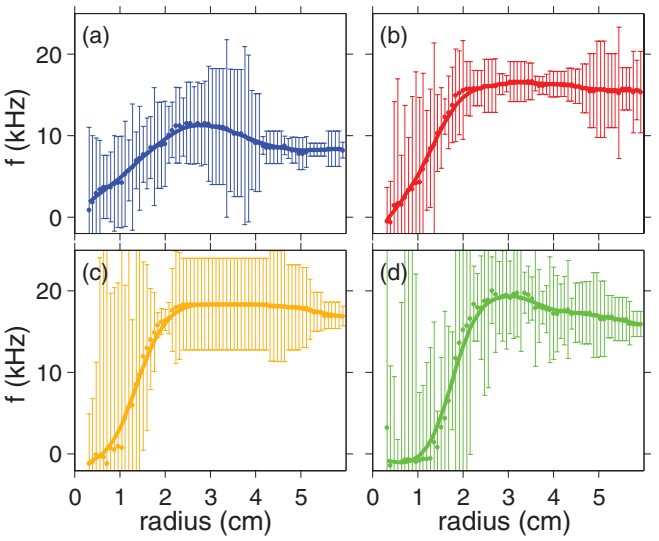

FIG. 7. (Color online) Measured radial evolution of the frequency for the mode numbers (a) $m = 1$, (b) $m = 2$, (c) $m = 3$, and (d) $m = 4$. The vertical lines indicate the error bars obtained from the temporal average of the frequency.

the radial evolution of the frequencies, which differs between the modes due to the drift wave dispersion.

The time series of the phases of the single Fourier modes at several radii have been evaluated. The average change of the phase angle with time corresponds to the average frequency $\langle \Delta\phi(r_i)/\Delta t \rangle = \langle \omega(r_i) \rangle$. Figure 7 shows the radial evolution of the frequency for the drift wave modes $m = 1-4$. The frequencies are Doppler shifted by approximately 1.5 kHz due to the background potential profile. For all modes the frequency is about zero close to the center and increases until it reaches the maximum values at approximately $r = 3$ cm. This agrees with the radially different frequencies observed in the temporal evolution of the decomposed modes in Fig. 5. Below $r = 8$ mm the resolution of the azimuthal pixel arrays becomes poor. Here a possible small misalignment of the center of the azimuthal pixel arrays may result in an error for the mode decomposition. Consequently, the error for the calculated frequency is larger close to the center. For the modes $m = 2$ and 3 the average frequency stays roughly constant from $r = 3$ cm up to larger radii. For $m = 1$ and 4 the frequency decreases toward larger radii. The measurements can be compared to the dispersion of the Hasegawa-Wakatani model, the standard model for three-dimensional drift wave turbulence [34,35]. The real part of the dispersion relation is equal to the Hasegawa-Mima equation (1). Figure 8 shows the frequencies [Fig. 8(a)] obtained from the camera measurement and the fits [Fig. 8(b)] to the $(E \times B)$-corrected Hasegawa-Mima equation (2). The input parameters $n_e(r)$, $T_e(r)$, and $\phi(r)$ are changed until the deviation between measured and calculated frequencies is minimal, while the fitted profiles are kept within the error bars of the profile measurements [Fig. 8(c)]. The calculated frequencies are in qualitative agreement with the camera measurements according to the following facts [see Figs. 8(a) and 8(b)]. The larger the mode number, the larger the maximum frequency is. For all modes the frequency increases from zero close to the center to its maximum in the density and

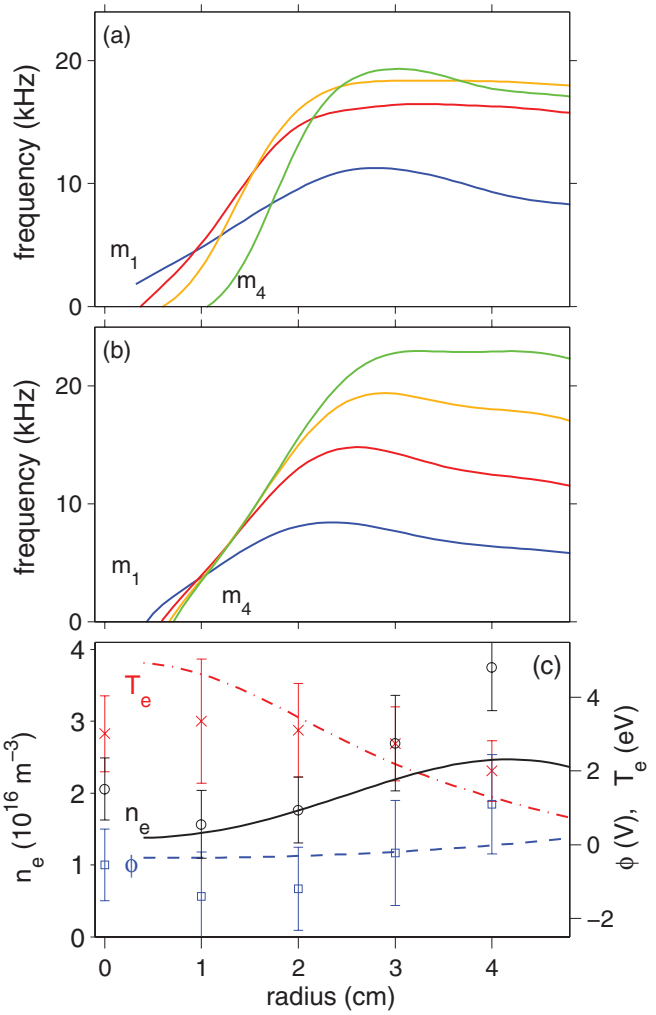

FIG. 8. (Color online) Measured and fitted radial evolution of the frequency: (a) measurement and (b) fits according to Eq. (2). (c) Profiles of the fits and the measurement for the plasma density (solid line and circles), electron temperature (dash-dotted line and crosses), and plasma potential (dashed line and squares).

temperature gradient region. At small radii the radial position, where the frequency starts growing, increases with the mode number. However, there are discrepancies in the quantitative values. The maximum frequencies of the fit for all modes are approximately 10% smaller. In the range $0.5 < r < 1.5$ cm the fitted frequencies of the modes, except for $m = 1$, increase similarly; in the measurement the frequencies of the modes are radially separated. At larger radii the fit deviates from the measurement especially for the modes $m = 2$ and 3; while the frequencies of these modes stay almost constant from $r = 3$ cm, they decay in the fit toward larger radii. At $r = 4$ cm the fitted density profile is outside the error bar of the measured profile. The discrepancies result from the large error of the measured frequencies, especially at smaller and larger radii (Fig. 7). Small deviations of the fitted profiles result in significant changes of the calculated frequencies since the drift wave dispersion is very sensitive to $n_e(r)$, $T_e(r)$, and $\phi(r)$. For radii $r > 3$ cm in particular the measured potential and density profile change considerably. Furthermore, the measured frequencies may be blurred in the radial and axial

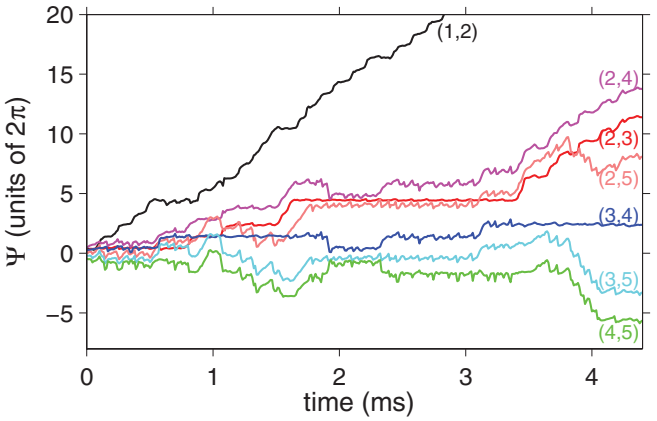

FIG. 9. (Color online) Phase differences of decomposed modes over the time of the transient.

directions due to the line of sight integration of the camera diagnostic. Also, the temporary locking of modes described in the following section may change the averaged frequency resulting in deviations from the dispersion relation.

A. Nonlinear coupling

The Fourier mode decomposition of the camera frames allows for calculating the phases of each Fourier mode component for each time instant. After subtraction of phases between different modes, coupling effects in weakly developed turbulent states become visible. Figure 9 depicts the differences between various mode phases in time measured at the radius $r = 3.2$ cm. In time three different regimes of coupling are observed: from 0 to 1.9 ms, weak turbulence; from 1.9 to 3.4 ms, temporary synchronization; and from 3.4 to 4.4 ms, turbulence. Curve (1,2), for the modes $m = 1$ and 2, exhibits a small ripple, which occurs with a certain beat frequency. The beat frequency is a sign of large detuning between coupled oscillators [36] and it results in a periodic pulling on the oscillators frequencies [37].

For other mode combinations beats are also observed, but, in addition, temporary synchronization occurs, indicated by a constant phase difference. Such interplay between periodic frequency pulling and transient phase locking can be considered an identifying characteristic of nonlinear mode coupling in weakly developed turbulence and can be simulated using the Kuramoto model. The Kuramoto model has served as a paradigm for interacting limit cycle oscillators with weak coupling in a dissipative system [12]. The system consists of N interacting oscillators, where each of them is perturbed by the others. The perturbation is added in the angular term of the harmonic oscillator Hamiltonian in action angle coordinates

$$\frac{d\theta_m}{dt} = \omega_m + \sum_{n=1}^{N} K_{m,n} \sin(\theta_m - \theta_n), \tag{3}$$

where ω_m is the natural frequency of oscillator m and $K_{m,n}$ are the elements of the perturbation strength matrix given by the other oscillators. The perturbation must have a value of $K_{m,n} < 1$ to ignore terms higher than $O(2)$. The dynamics of the Kuramoto system can be visualized by considering two

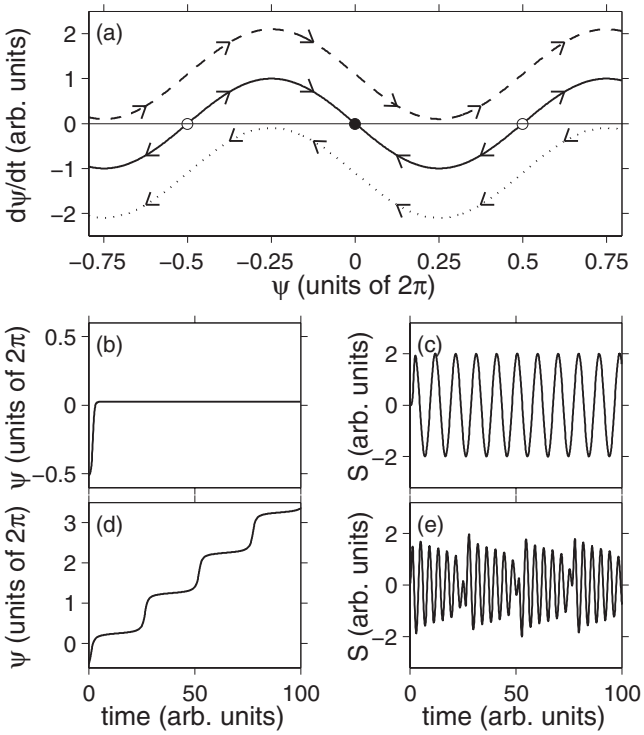

FIG. 10. (a) Trajectories of the two-oscillator Kuramoto model with fixed points $[\Delta\omega = \omega_2 - \omega_1 = 0,\ \sum K = K_{1,2} + K_{2,1} = 1$ (solid line)] and without fixed points $[\Delta\omega = \{1.1, -1.1\}, \sum K = 1$ (dashed and dotted lines)]. Evolution of the phase differences Ψ between two oscillators and the coupled signal S for (b) and (c) the phase locked case and (d) and (e) the quasiperiodic case (periodic pulling).

interacting oscillators, which yield an equation for the phase difference $\psi = \theta_2 - \theta_1$:

$$\frac{d\psi}{dt} = (\omega_2 - \omega_1) - (K_{1,2} + K_{2,1})\sin(\psi). \tag{4}$$

Figure 10(a) shows three trajectories of Eq. (4) in the phase space $\{\psi, d\psi/dt\}$. It exhibits attracting fixed points (solid black circle) as long as $\omega_2 - \omega_1 < K_{1,2} + K_{2,1}$. Figures 10(b) and 10(c) show a numerical solution of Eq. (4) for the time evolution of the phase difference ψ for the case in which a fixed point is present. It is found that the phase difference rapidly converges to a constant value and the coupled signal of both oscillators is periodic. When $\omega_2 - \omega_1 > K_{1,2} + K_{2,1}$ the trajectory is larger than $d\psi/dt = 0$ and there are no fixed points in phase space [Fig. 10(a)]. If the trajectory is then near the axis, the phase difference changes on two different time scales: If $d\psi/dt$ is close to zero the phase difference changes slowly and is almost constant followed by an abrupt jump, during $d\psi/dt \gg 0$.

This phase slippage appears periodically and the oscillators exhibit a quasiperiodic motion [Figs. 10(d) and 10(e)]. This is what is often called periodic pulling [37–39]. If the trajectory is at values much larger than $d\psi/dt = 0$ due to a higher frequency difference, the periodic slippage becomes more and more frequent until the phase difference becomes a straight line with a constant slope and the oscillators act independently. The parameter space $\{\omega_2 - \omega_1, K_{1,2} + K_{2,1}\}$ for the region of entrainment has a symmetric, tonguelike shape (an Arnol'd tongue). If higher-order terms are taken into account in Eq. (3), deviations in the tongue symmetry are observed due to nonlinear effects. Note that for the case of a simple forced oscillator Eq. (4) becomes [40]

$$\frac{d\psi}{dt} = (\omega_f - \omega_0) - K_{f,0}\sin(\psi), \tag{5}$$

where $\psi = \theta_f - \theta_0$ is the phase difference between the oscillator and the periodic forcing term and $K_{f,0}$ is the forcing amplitude. This equation can be used as a simple model for the quasiperiodicity by external entrainment and the observation of symmetric tongues at low forcing amplitudes as observed in coherent states in magnetized plasma columns [38,41]. Here the entrainment tongues become asymmetric close to moderate forcing amplitudes.

Phase locking has also been studied in systems exhibiting chaotic dynamics (in Ref. [42], for example, the Rössler system was used) where phase slippage was also observed. In these dynamical systems the phase slippage is nonperiodic. Instead it appears at erratic times, apparently being stochastic. Experiments in plasma discharge tubes [43] and magnetized plasma columns in weakly developed turbulent states [41,44,45] have shown similar behavior.

The simplest system with erratic phase slippage is a Langevin-type extension of the Kuramoto model

$$\frac{d\theta_m}{dt} = \omega_m + \xi(\sigma,t) + \sum_{n=1}^{N} K_{m,n}\sin(\theta_m - \theta_n), \tag{6}$$

where $\xi(\sigma,t)$ is a noise term and σ is its variance due to a Gaussian probability distribution with $\langle\xi(\sigma,t)\rangle = 0$ and $\langle\xi(\sigma,t)\xi(\sigma,t')\rangle = \delta(t - t')$. As the variance is larger, phase slippage becomes more frequent [43] until the phase difference resembles a random walk. An example with six interacting oscillators, all connected to each other, can be seen in Fig. 11(a) . Here the coupling coefficients are generated by a random matrix according to a Gaussian probability distribution and the variance is changed to simulate the three regimes observed in the measurement. The only boundary condition is a reduction of the coupling coefficients of the $m = 1$ mode by a factor of 0.1 since the measurement exhibits weak coupling of the $m = 1$ mode with other modes. It is found that the experimentally observed temporal evolution of the phase differences in the three regimes can be reproduced by applying the random matrix to the Kuramoto equation.

Recent studies in network dynamics have led to the search for methods to infer the network topology of interacting oscillators. We have applied the method proposed in Ref. [46] for inferring the network topology [Fig. 11(b)]. In this way the coupling matrix $K_{m,n}$ is calculated from Eq. (3) from the measured time series of the phase differences between the modes by an error minimization procedure. Some experimentally observed features of the growth of the phase difference between modes can be reproduced, e.g., the similar growth between the modes (2,3) and (2,5). There is a high stability of mode pairs (3,4), which is also observed in the measurement [Fig. 9].

Using the Kuramoto model as an energy dissipative system for modeling the internal phase coupling in drift wave

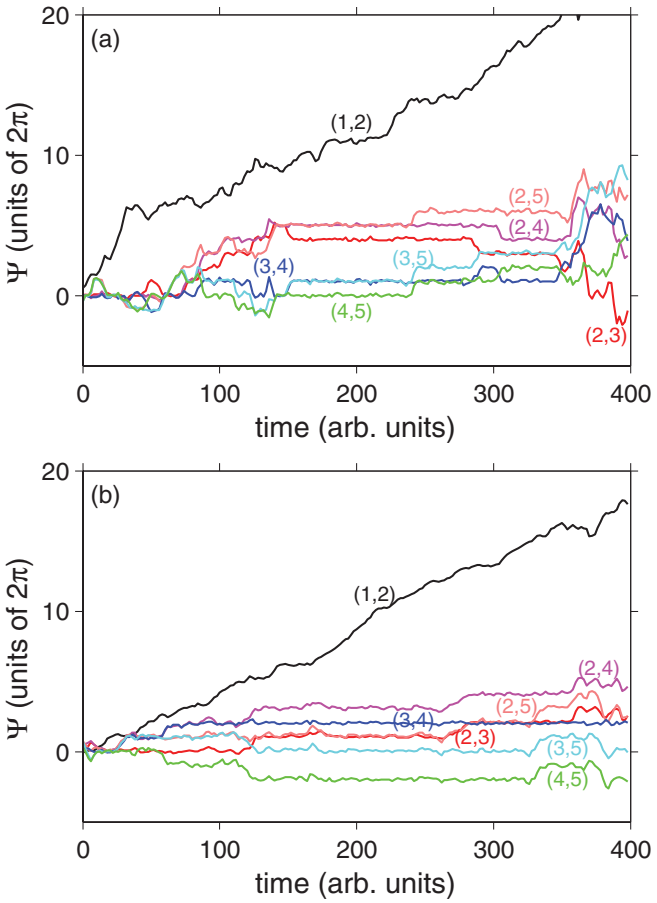

FIG. 11. (Color online) Calculated phase differences due to the Kuramoto model for five interacting oscillators with arbitrary coupling constants derived from (a) a random coupling matrix and (b) a coupling matrix obtained from the measurements.

turbulence yields considerable agreement with the measurement. Several open-loop control experiments of drift waves demonstrate that an artificially driven drift wave mode couples to certain single drift wave modes [4,25,41,44,45,47,48]. Nonlinear coupling effects such as frequency pulling, synchronization, and Arnol'd tongues have been observed. The parallel currents $j_{\parallel}$ are the important link in the coupling chain between the artificial and driven modes [4,41,44]. If a single mode shows synchronization to an external artificial mode, then also two interacting modes would have the tendency to mutually synchronize. Consequently, it is assumed that fluctuations of the parallel currents, caused by one drift wave mode, couple to potential and density fluctuations of another drift wave mode according to the equation system for density and potential fluctuations of the Hasegawa-Wakatani model [34,49]. Indeed, Fig. 9 demonstrates internal periodic pulling and synchronization of drift wave modes in weakly developed turbulence. We assume that the coupling matrix $K_{m,n}$ can be regarded as the individual coupling strength between the parallel currents of the single drift wave modes. The noise term ξ may represent the perturbations from different plasma fluctuations. Furthermore, temporary synchronization of modes in turbulence may influence the cross-field transport. However, for precise conclusions more well-defined investigations need to be done.

III. CONCLUSION

In the present work we have investigated spatiotemporal drift wave dynamics by measuring visible light fluctuations in the azimuthal cross section of a linear magnetized plasma. It is demonstrated that the Fourier decomposition of the cross section is a useful tool for the investigation of the dynamics of coupled modes in turbulence. The evolution of the fluctuation amplitude of each mode can be analyzed in temporal and radial dimension. Based on this procedure, the radial evolution of the frequency of the decomposed drift wave modes has been evaluated from measurements in weakly developed drift wave turbulence. It shows that the measurements are in agreement with calculations of the real part of the Hasegawa-Wakatani dispersion relation. Observed radial breaks of the mode structure are related to the radial change of the frequency. The modes exhibit azimuthal and radial components due to the radial breaks and the spiral-like mode structure.

In Ref. [50] it is shown that spiral structures are a general phenomenon in magnetized rotating plasmas. However, the origin of the spiral-like mode structure in the present work is ambiguous. Using the Mirabelle device and other thermionic plasma devices, spiral structures have been observed for flutelike modes, where centrifugal effects are believed to be responsible [51–53]. For drift waves, spiral-like structures have been observed in collisional plasmas [54]. Here the explanation is a radial dependence of the Coulomb collisionality. (Electron collisions determine the phase shift between potential and density fluctuations as well as the $E \times B$ drift advection.) In the present work, the collisionality is low $\nu_{ei}/\omega_{ci} \approx 0.05$; in addition, the core fluctuations lag behind the edge fluctuations, in contrast to the observations in Refs. [50–54]. However, the observed spiral structure can also be a measurement artifact. Since the camera is not a pure two-dimensional diagnostic, it maps not only the azimuthal cross section but the three-dimensional structure of drift waves due to the line of sight integration of light (approximatively one-third of the plasma column). In this way, the view along the magnetic field, i.e., along the parallel drift wave structure, may distort the azimuthal mode structure, resulting in spiral arms of maxima and minima.

The coupling of modes is studied by evaluating the temporal dependence of the phase differences between different mode numbers. It turns out that for certain temporal intervals modes are locked and for other intervals modes are unlocked. The effect of synchronization and desynchronization has been investigated by a simple model of nonlinearly coupled oscillators. Synchronization and desynchronization of coupled oscillators are found only if the additional noise level increases above a certain threshold. Below that level, the oscillators stay synchronized as soon as synchronization sets in. In drift wave turbulence, the noise may arise from the large number of other modes present or from fluctuations due to other instabilities in the plasma column, e.g., beam-plasma interactions [55,56].

ACKNOWLEDGMENTS

We gratefully acknowledge useful discussions with Dr. Volker Naulin. Financial support was received from the French National Research Agency through Contract No. ANR-07-BLAN-0187-01.

[1] W. Horton, Rev. Mod. Phys. **71**, 735 (1999).
[2] G. R. Tynan, A. Fujisawa, and G. McKee, Plasma Phys. Controlled Fusion **51**, 113001 (2009).
[3] A. Latten, T. Klinger, A. Piel, and Th. Pierre, Rev. Sci. Instrum. **66**, 3254 (1995).
[4] C. Schröder, T. Klinger, D. Block, A. Piel, G. Bonhomme, and V. Naulin, Phys. Rev. Lett. **86**, 5711 (2001).
[5] N. Krause, C. Lechte, J. Stöber, U. Stroth, E. Ascasibar, J. Alonso, and S. Niedner, Rev. Sci. Instrum. **73**, 3474 (2002).
[6] K. Kamiya *et al*., Plasma Phys. Controlled Fusion **49**, S43 (2007).
[7] G. Y. Antar, J. H. Yu, and G. Tynan, Phys. Plasmas **14**, 022301 (2007).
[8] S. Oldenbürger, C. Brandt, F. Brochard, N. Lemoine, and G. Bonhomme, Rev. Sci. Instrum. **81**, 063505 (2010).
[9] T. H. Stix, Phys. Fluids **12**, 633 (1969).
[10] F. Y. Gang, P. H. Diamond, J. A. Crotinger, and A. E. Koniges, Phys. Fluids B **3**, 955 (1991).
[11] A. Hasegawa and Y. Kodama, Phys. Rev. Lett. **41**, 1470 (1978).
[12] Y. Kuramoto, in *Chemical Oscillations, Waves and Turbulence* (Dover, New York, 2003), p. 69.
[13] S. H. Strogatz, in *Nonlinear Dynamics and Chaos* (Addison-Wesley, Reading, MA, 1994), p. 104.
[14] D. Hansel, G. Mato, and C. Meunier, Europhys. Lett. **23**, 367 (1993).
[15] T. Gregor, K. Fujimoto, N. Masaki, and S. Sawai, Science **328**, 1021 (2010).
[16] E. Ott and T. M. Antonsen, Chaos **18**, 037113 (2008).
[17] M. Timme, Europhys. Lett. **76**, 367 (2006).
[18] S. H. Strogatz, Physica D **143**, 1 (2000).
[19] Th. Pierre, G. Leclert, and F. Braun, Rev. Sci. Instrum. **58**, 6 (1987).
[20] E. Gravier, F. Brochard, G. Bonhomme, Th. Pierre, and J. L. Briançon, Phys. Plasmas **11**, 529 (2004).
[21] S. Oldenbürger, Ph.D. thesis, Institute Jean Lamour, Nancy, 2010 [http://www.scd.uhp-nancy.fr/docnum/scd_t_2010_0024_oldenburger.pdf].
[22] E. Gravier, X. Caron, G. Bonhomme, and Th. Pierre, Phys. Plasmas **6**, 1670 (1999).
[23] E. Gravier, X. Caron, G. Bonhomme, Th. Pierre, and J. L. Briançon, Eur. Phys. J. D **8**, 451 (2000).
[24] F. Brochard, E. Gravier, and G. Bonhomme, Phys. Plasmas **12**, 062104 (2005).
[25] F. Brochard, G. Bonhomme, E. Gravier, S. Oldenbürger, and M. Philipp, Phys. Plasmas **13**, 052509 (2006).
[26] F. F. Chen, in *Introduction to Plasma Physics and Controlled Fusion* (Plenum, New York, 1984), p. 219.
[27] F. F. Chen, Phys. Fluids **22**, 2346 (1979).
[28] A. Hasegawa and K. Mima, Phys. Rev. Lett. **39**, 205 (1977).
[29] T. Klinger, A. Latten, A. Piel, G. Bonhomme, and Th. Pierre, Plasma Phys. Controlled Fusion **39**, 145 (1997).
[30] R. F. Ellis and E. Marden-Marshall, Phys. Fluids **22**, 2137 (1979).
[31] R. F. Ellis, E. Marden-Marshall, and R. Majeski, Plasma Phys. **22**, 113 (1980).
[32] C. Schröder, O. Grulke, T. Klinger, and V. Naulin, Phys. Plasmas **12**, 042103 (2005).
[33] O. Grulke, T. Klinger, and A. Piel, Phys. Plasmas **6**, 788 (1999).
[34] A. Hasegawa and M. Wakatani, Phys. Rev. Lett. **50**, 682 (1983).
[35] M. Wakatani and A. Hasegawa, Phys. Fluids **27**, 611 (1984).
[36] C. Hayashi, in *Nonlinear Oscillations in Physical Systems* (Princeton University Press, Princeton, 1964), p. 302.
[37] M. E. Koepke and D. M. Hartley, Phys. Rev. A **44**, 6877 (1991).
[38] T. Klinger, F. Greiner, A. Rohde, A. Piel, and M. E. Koepke, Phys. Rev. E **52**, 4316 (1995).
[39] M. E. Koepke, A. Dinklage, T. Klinger, and C. Wilke, Phys. Plasmas **8**, 1432 (2001).
[40] A. Pikovsky, M. Rosenblum, and J. Kurths, in *Synchronization* (Cambridge University Press, Cambridge, 2001), p. 181.
[41] C. Brandt, O. Grulke, and T. Klinger, Phys. Plasmas **17**, 032304 (2010).
[42] E. Rosa Jr, E. Ott, and M. H. Hess, Phys. Rev. Lett. **80**, 1642 (1998).
[43] A. Pikovsky, M. Rosenblum, and J. Kurths, Int. J. Bifurcation and Chaos **10**, 2291 (2000).
[44] C. Brandt, O. Grulke, and T. Klinger, Plasma Phys. Controlled Fusion **52**, 055009 (2010).
[45] D. Block, A. Piel, C. Schröder, and T. Klinger, Phys. Rev. E **63**, 056401 (2001).
[46] S. G. Shandilya and M. Timme, New J. Phys. **13**, 013004 (2011).
[47] D. Block, C. Schröder, T. Klinger, and A. Piel, Contrib. Plasma Phys. **41**, 455 (2001).
[48] C. Schröder, T. Klinger, G. Bonhomme, D. Block, and A. Piel, Contrib. Plasma Phys. **41**, 461 (2001).
[49] V. Naulin and K. H. Spatschek, Phys. Rev. E **55**, 5883 (1997).
[50] M. Kono and M. Y. Tanaka, Phys. Rev. Lett. **84**, 4369 (2000).
[51] M. Matsukuma, Th. Pierre, A. Escarguel, D. Guyomarc'h, G. Leclert, F. Brochard, E. Gravier, and Y. Kawai, Phys. Lett. A **314**, 163 (2003).
[52] Th. Pierre, A. Escarguel, D. Guyomarc'h, R. Barni, and C. Riccardi, Phys. Rev. Lett. **92**, 065004 (2004).
[53] R. Barni, C. Riccardi, Th. Pierre, G. Leclert, A. Escarguel, D. Guyomarc'h, and K. Quotb, New J. Phys. **7**, 225 (2005).
[54] C. Schröder, O. Grulke, T. Klinger, and V. Naulin, Phys. Plasmas **11**, 4249 (2004).
[55] J. H. Malmberga and C. B. Wharton, Phys. Fluids **12**, 2600 (1969).
[56] H. Ikezi, R. P. H. Chang, and R. A. Stern, Phys. Rev. Lett. **36**, 1047 (1976).